The thermodynamic properties of hydrated γ-Al$_2$O$_3$ nanoparticles

Elinor C. Spencer, Baiyu Huang, Stewart F. Parker, Alexander I. Kolesnikov, Nancy L. Ross, and Brian F. Woodfield

View Online   Export Citation   CrossMark

The thermodynamic properties of hydrated γ-Al$_2$O$_3$ nanoparticles

Elinor C. Spencer,[1] Baiyu Huang,[2] Stewart F. Parker,[3] Alexander I. Kolesnikov,[4]
Nancy L. Ross,[1] and Brian F. Woodfield[2]

[1]*Department of Geosciences, Virginia Tech, Blacksburg, Virginia 24061, USA*
[2]*Department of Chemistry and Biochemistry, Brigham Young University, Provo, Utah 84602, USA*
[3]*ISIS Facility, STFC Rutherford Appleton Laboratory, Chilton, Didcot, Oxon OX11 0QX, United Kingdom*
[4]*Chemical and Engineering Materials Division, Oak Ridge National Laboratory, P.O. Box 2008,*
Oak Ridge, Tennessee 37831, USA

In this paper we report a combined calorimetric and inelastic neutron scattering (INS) study of hydrated γ-Al$_2$O$_3$ (γ-alumina) nanoparticles. These complementary techniques have enabled a comprehensive evaluation of the thermodynamic properties of this technological and industrially important metal oxide to be achieved. The isobaric heat capacity (C_p) data presented herein provide further critical insights into the much-debated chemical composition of γ-alumina nanoparticles. Furthermore, the isochoric heat capacity (C_v) of the surface water, which is so essential to the stability of all metal-oxides at the nanoscale, has been extracted from the high-resolution INS data and differs significantly from that of ice–Ih due to the dominating influence of strong surface-water interactions. This study also encompassed the analysis of four γ-alumina samples with differing pore diameters [4.5 (**1**), 13.8 (**2**), 17.9 (**3**), and 27.2 nm (**4**)], and the results obtained allow us to unambiguously conclude that the water content and pore size have no influence on the thermodynamic behaviour of hydrated γ-alumina nanoparticles. © *2013 AIP Publishing LLC*. [http://dx.doi.org/10.1063/1.4850636]

I. INTRODUCTION

Alumina (Al$_2$O$_3$) exhibits complex polymorphism at the nanoscale that is primarily controlled by thermodynamic considerations.[1,2] In particular, the surface energies of the different phases of alumina play a pivotal role in determining the relative stabilities of the phases as a function of particle size. Coarse crystalline alumina predominately exists as the α form (corundum) under standard conditions, however, when the surface area of the particles exceeds the threshold value of ~125 m^2/g the γ form becomes energetically more stable. This is a direct consequence of the lower surface energy of the γ form relative to the α polymorph. In fact, alumina exists in numerous polymorphic forms (α, χ, γ, δ, η, θ, and κ-Al$_2$O$_3$), and the routes by which these forms interconvert as the particles grow during synthesis have been the subject of extensive investigation.[3,4] It is known that surface water (both chemi- and physisorbed) is essential for stabilising alumina nanoparticles, and the higher the surface energy associated with a particular polymorph the more critical the role of the surface water becomes.[1,5–7] Stripping the surface water from the alumina nanoparticles causes particle coarsening and can induce undesired phase transitions.[7]

Nonetheless, the diversity that is inherent in the physical nature of alumina nanoparticles has been exploited to generate particles suitable for a range of applications. It has been shown that the inclusion of alumina nanoparticles in engine coolant fluid,[8] plastics,[9] and liquid crystal media[10] can drastically alter the mechanical and dynamic behaviour of such commercially relevant materials. Indeed, by adjusting the particle size the agglomeration behaviour of alumina particles can be tailored to create alumina-based additives that

have the ability to improve the efficiency of lubricants by as much as 50%.[11,12] Moreover, the versatility of alumina nanoparticles is evidenced by the fact that as well as being lubricant additives, they are also employed as abrasive materials either in pure form or as composites.[13,14] As the size of the particles can be controlled easily the surface area of alumina nanoparticles can also be customised. Consequently, alumina materials are also being developed for environmental remediation processes such as the removal of metals from the watercourse,[15–18] and as catalyst supports for a variety of industrially important chemical reactions such as CO and methane oxidation,[19–21] and the hydrolytic dehydration of ammonia borane.[22] In addition, the high surface area and absorption properties of alumina nanoparticles have been utilised for the chromatographic separation of clinical grade ^{188}W/^{188}Re radioisotopes for pharmaceutical purposes.[23]

In this paper we discuss in detail the thermodynamic properties of this important metal oxide at the nanoscale. By combining inelastic neutron scattering (INS) techniques and calorimetric measurements a comprehensive understanding of the heat capacity of the particles and surface water has been achieved. Moreover, we offer further insights into the chemical composition of γ-Al$_2$O$_3$.

II. EXPERIMENTAL METHODS

A. Synthesis

The alumina samples employed in this study were synthesised by a proprietary method.[24–28] For sample **1**, 22.516 g of Al(NO$_3$)$_3$ · 9H$_2$O and 14.235 g of NH$_4$HCO$_3$ were mixed in a mortar and ground vigorously with a pestle for 20 min at room temperature. For sample **2**, 20.031 g of aluminium

iso-propoxide was mixed with 12.36 ml of distilled water (H_2O/Al molar ratio 7:1) with a mortar and pestle for 15 min. For sample **3**, 24.158 g of aluminium *sec*-butoxide was mixed with 8.83 ml of distilled water (H_2O/Al molar ratio 5:1) with a mortar and pestle for 15 min. For sample **4**, the intermediate obtained during the synthesis of sample **2** was rinsed with 200 ml of *sec*-butanol over a filter and under house vacuum, and then allowed to gel for 16 h. The resultant intermediates, or precursors, were then thermally treated in a Thermo Scientific Lindburg Blue M Oven. The samples were heated to 973 K at a ramp rate of 2.33 K/min and then held at this temperature for 2 h. This slow ramp was employed to (i) avoid rapid dehydration and thus ensure uniform pore construction and (ii) to ensure uniform heat transfer to achieve enhanced sample homogeneity, and to avoid rapid grain growth. After the 2 h hold the samples were cooled to room temperature at a ramp rate of 10 K/min.

B. Characterisation methods

All samples were characterised by several analytical techniques. The water contents of the samples were determined by thermogravimetric and differential thermal analyses (TGA-DTA) performed on a Netzsch STA 409PC instrument; the alumina sample ($\sim$30 mg) was placed in a Pt crucible and heated at 3 K/min over the 25–1473 K temperature range while held under flowing He. Transmission electron micrographs (TEM) were collected with a FEI Philips Technai F20 Analytical STEM operating at 200 kV. For these measurements the alumina samples were first dispersed in ethanol, and a single drop of this solution was placed on a formvar/carbon film supported by a 200-mesh Cu grid. The ethanol was allowed to evaporate before high-resolution images were recorded. The phase purity and average particle sizes of the samples were confirmed by application of the Scherrer formula to the powder X-ray diffraction (PD-XRD) data collected on a A PANalytical X'Pert Pro diffractometer utilizing monochromated Cu-radiation (λ = 1.5406 Å). The particle sizes determined from the PD-XRD data were consistent with those obtained from the TEM measurements. Nitrogen adsorption analyses were carried out at 77 K with a MicromeriticsTristar 3020 apparatus. Prior to measurement the samples were degassed overnight at 473 K under flowing nitrogen. Specific surface areas (SA) were calculated by the Brunauner-Emmett-Teller (BET) method with a P/P_0 range between 0.05 and 0.2.[29] Pore volumes (PV) were calculated from the adsorption isotherm at the relative pressure of 0.990, and the average pore diameters (APD) were determined by the SPG model utilising either the adsorption branch or desorption branch of the isotherm depending on the type of isotherm hysteresis.[30,31] The adsorption branch was used for samples with a pore width less than 10 nm, whereas the desorption branch was used for those samples with a pore width greater than 10 nm. Pore size distributions (PSD) and mesopore volumes were calculated from the adsorption and desorption data by a newly developed method involving slit pore geometry for the Kelvin equation and structural corrections for the areas and volumes, while the data were fitted with a lognormal distribution functions.[32]

C. Calorimetric measurements

Heat capacity measurements were performed with a Quantum Design PPMS in zero magnetic field, with logarithmic spacing in the 2–100 K temperature range, and at 10 K intervals over the 100–300 K, and at 0.1 K intervals in the temperature region of a phase transition. The accuracy of these heat capacity measurements was determined by analysis of powdered copper and benzoic acid, and was found to be $\pm$1% in the 22–300 K range and $\pm$2%–5% below 22 K.[31] The powdered alumina samples were measured by a new technique developed in our laboratory for powdered samples that use a PPMS calorimeter. The details of sample mounting and the heat capacity experimental procedures can be found in our recent publications.[31,33]

D. Low energy (0–120 meV) INS measurements

Low temperature (20 K) INS spectra for all Al_2O_3 samples were collected over the 0–200 meV energy range on the TOSCA spectrometer at the ISIS Facility (pulsed neutron source) at the Rutherford Appleton Laboratory (Oxford, UK).[34] TOSCA is an inverse geometry time-of-flight (TOF) spectrometer with a wide energy range of incident neutrons and fixed final energy, and has excellent resolution ($\Delta E/E \approx 1.5\%$) at low energy transfers (<200 meV).

The dynamical structure factor data [$S(E,Q)$] (provided in the SI) that were collected on TOSCA were converted to the generalized vibrational density of states [$G(E)$] by application of the following equation:[35,36]

$$G(E) = \frac{S(E, Q) \cdot E}{Q^2[n(E, T) + 1]}, \qquad (1)$$

Where E is the energy transfer; T is the temperature; Q is the magnitude of momentum transfer that was calculated with Eq. (2); and $n(E,T)$ is the population Bose factor that was calculated with Eq. (3):

$$Q^2 = \frac{2m}{\hbar^2}[E_f + E + E_f - 2\cos(\varphi)\sqrt{(E_f + E)E_f}], \quad (2)$$

where m is the neutron mass; $\hbar$ is the Dirac's constant; E_f is the final energy; and φ is the scattering angle. E_f is a constant and for TOSCA and the average values for the forward and backscattering detectors are equal to 3.35 meV and 3.32 meV, respectively. The incident energy is given by $E_i = E_f + E$:

$$n(E, T) = \left[\exp\left(\frac{E}{kT}\right) - 1\right]^{-1}, \qquad (3)$$

where k is the Boltzmann's constant.

The data were corrected for thermal effects with the Debye-Waller factor [$W(Q)$], which is described by the expression $W(Q) = \exp(-BQ^2)$, where B is the mean squared displacement of the atoms: $B = \langle u^2 \rangle$. However, there is no direct way to determine B from the INS data, so for the processing of the data presented herein B was approximated to 0.01 Å^2, a value that is reasonable for atomic displacements at very low temperatures.

The low energy regions (0–3 meV) of the spectra are obscured by the elastic peaks and consequently a simple Debye model of the form $G(E) = AE^2$ was applied in these

TABLE I. Physical properties of alumina samples **1–4**.

Sample	d (nm)	Surface area (m^2/g)	Pore diameter (nm)	Pore volume (cm^3/g)	H_2O molecules *per* nm^2	Formula
1	3.3	258 ± 13	4.5 ± 1.4	0.35 ± 0.05	16	$Al_2O_3 \cdot 0.69\ H_2O$
2	3.4	293 ± 15	13.8 ± 3.4	1.21 ± 0.07	12	$Al_2O_3 \cdot 0.59\ H_2O$
3	3.3	325 ± 17	17.9 ± 5.6	1.71 ± 0.09	9	$Al_2O_3 \cdot 0.50\ H_2O$
4	2.7	235 ± 12	27.2 ± 8.6	1.19 ± 0.07	12	$Al_2O_3 \cdot 0.48\ H_2O$

regions of the spectra,[37,38] where A is a constant that is inversely proportional to the Debye frequency and was set at a value that ensured the E^2 was appropriately scaled to the spectrum (i.e., A also contains an arbitrary scaling component). Due to the much larger neutron scattering cross section of hydrogen atoms compared to other constituent atoms (Al an O), the INS spectra mainly represent the vibrations of the hydrogen within the surface water. Therefore, the spectra were then scaled such that the areas of the translational (0–40 meV) and librational (50–120 meV) sections of the spectra were each equal to three, corresponding to the three degrees of translational and librational freedom of water.[39] The final outcome from this data processing procedure is the vibrational density of states (VDOS) for the hydration layers.

E. High energy (0–600 meV) INS measurements

Low temperature (7 K) INS data over the 0–600 meV energy range were collected for selected samples (**1**, **3**, and **4**) on the fine energy high resolution direct geometry chopper spectrometer SEQUOIA located at the Spallation Neutron Source (SNS) at Oak Ridge National Laboratory (ORNL).[40,41] Data were collected with an incident energy (E_i) of 600 meV selected by the Fermi chopper rotating with 600 Hz, and scattering neutrons of all energies were registered by position sensitive detectors in wide range of scattering angles, from $-30°$ to $+60°$ in the horizontal plane and $\pm18°$ in the vertical directions. The collected neutron scattering data were transformed from the time-of-flight and instrument coordinates to the dynamical structure factor $S(Q,E)$ and then to the generalized VDOS, $G(E)$. The background spectra for the empty container were measured under the same conditions and subtracted from the sample data.

III. RESULTS AND DISCUSSION

A. Sample characterisation

The results from the various sample characterisation analyses are summarised in Table I. PD-XRD patterns and PSD plots for all samples employed in this study are provided in the supplementary material.[63] The individual alumina nanoparticles are arranged such that a 3D mesoporous material results. The pores within this complex structure may exhibit diversity with respect to their geometry, surface roughness, exposed surface defects, and of course with respect to their dimensions. The individual alumina samples employed in this study have uniform particle sizes with well-defined pore volumes and diameters (see the supplementary material).[63] Although the individual samples are uniform, there is, however, a systematic change in the pore dimensions (i.e., volume and diameter) between the samples. The number of water molecules per nm^2 of alumina surface was estimated for each sample based on the measured surface areas and water contents, and it is reassuring to note that the samples have equivalent levels of water coverage, and thus the results from the thermodynamic measurements detailed below are directly comparable. Consequently, the influence of pore sizes on the heat capacity of alumina nanoparticles can be assessed.

TEM images of alumina samples **1–4** are provided in Fig. 1. It is interesting to note that, despite the similarity in the size of the particles, their morphologies differ. The agglomerated nanoparticles in **1** are spherical in shape and closely packed, an arrangement that is consistent with this sample having the smallest pore diameter of all the samples investigated. Conversely, samples **2–4** are plate-like in nature, and the particles are more loosely packed than observed in **1**. Again, this is consistent with these samples having large pore diameters than in **1**. The difference in sample morphologies is probably due to subtle variations in the synthetic procedures employed in their preparation. The modification of

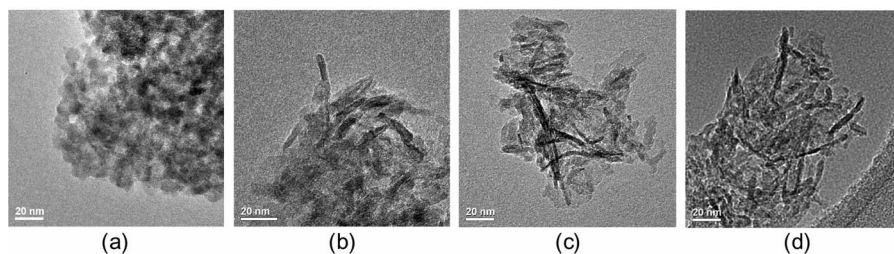|			
(a)	(b)	(c)	(d)

FIG. 1. TEM images of alumina agglomerated nanoparticles: (a) sample **1**; (b) sample **2**; (c) sample **3**; (d) sample **4**. The white scale at the bottom left of each image corresponds to a length of 20 nm. Notice the spherical morphology for **1**, and the plate-like morphologies of **2–4** (rod-shaped entities are likely to be plate-shaped particles viewed edge-on).
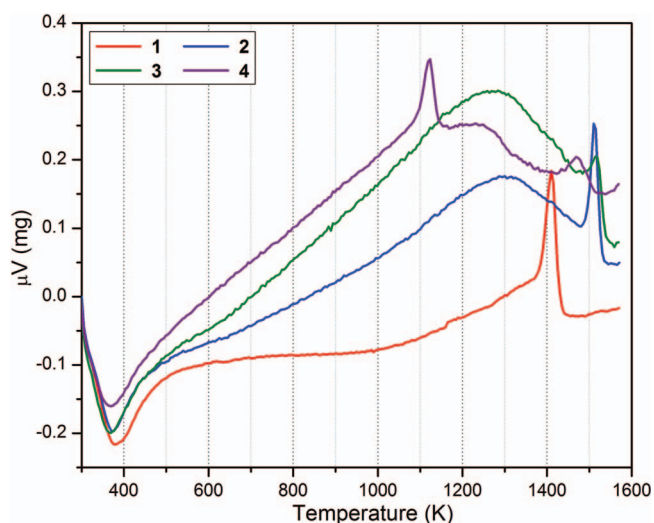
FIG. 2. DTA traces for alumina samples **1–4**. For all samples the peak corresponding to the $\gamma \rightarrow \alpha$ phase transition occurs at a temperature >1400 K.

synthesis conditions for the selected growth of nanoparticles with desirable morphologies has been previously documented for these alumina samples, TiO_2, Co_3O_4, and ZnO.[27,28,42–44] Such methods rely on the optimization of the synthetic conditions to induce the preferential growth of specific faces of the crystalline nanoparticles, which is possible if the relative surface energies of the faces differ. In the case of γ-alumina, with tetragonally distorted cubic crystal symmetry, the following relationship has been deduced for the energies of the different crystal faces: {001} < {111} < {110}.[3,45,46]

The DTA trace (Fig. 2) for sample **1** indicates that the $\gamma \rightarrow \alpha$ phase transition, which is accompanied by particle growth, for this alumina sample occur at ~1410 K, but for **2** and **3** the transition temperature is higher (>1510 K). In the case of sample **4** additional transitions are observed prior to the $\gamma \rightarrow \alpha$ transition at ~1470 K; this would suggest that this material undergoes a more complex range of transitions

potentially involving multiple alumina phases and/or particle reorientations, than occur for **1–3**, for example, $\gamma \rightarrow \delta$ and $\delta \rightarrow \theta$ transitions. These nuances in the DTA data for alumina samples **1–4** may arise due to differences in the contact distances been the particles; a similar effect has been observed in Fe_2O_3 nanoparticles in which number of interparticle contacts has a profound effect on the $\gamma \rightarrow \alpha$ transition temperature.[47] In the case of Fe_2O_3 the greater the number of contacts the lower the transition temperature, this is akin to our finding that the γ-alumina sample with the closest packed particles (**1**) converts to the α form at a lower temperature relative to those observed for alumina samples with larger pore diameters.[4]

B. Thermodynamics of alumina nanoparticles

The low temperature regime of the heat capacity (<10 K) curves (Fig. 3) are primarily associated with the lattice vibrations of the alumina nanoparticles; consequently, they are best fitted with a harmonic-lattice model that comprises odd powers of temperature (T):[48]

$$C_{Lat} = \sum_{n=3,5,7..} B_n T^n + \gamma T. \tag{4}$$

The linear term γT is a necessary inclusion in Eq. (4) if the non-conducting alumina particles contain isolated atomic vacancies within their crystalline lattices.

The molar isobaric heat capacity (C_p) data collected over the intermediate temperature range (5–75 K) are best described by a simple polynomial expression:

$$C_{Emp} = \sum_{n=0 \rightarrow 6} k_n T^n. \tag{5}$$

The high temperature C_p data (>50 K) have been successfully fitted with a combined Debye-Einstein specific-heat function that accounts for the contribution of the optical and acoustic phonon modes of the alumina lattice to the heat capacity of the nanoparticles; this expression takes the following
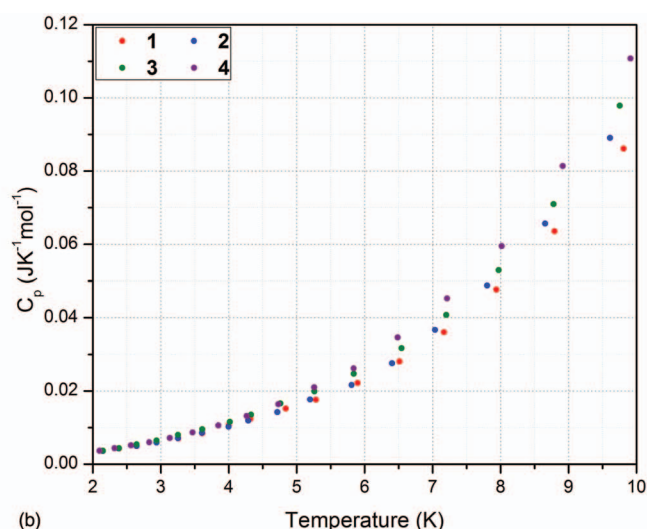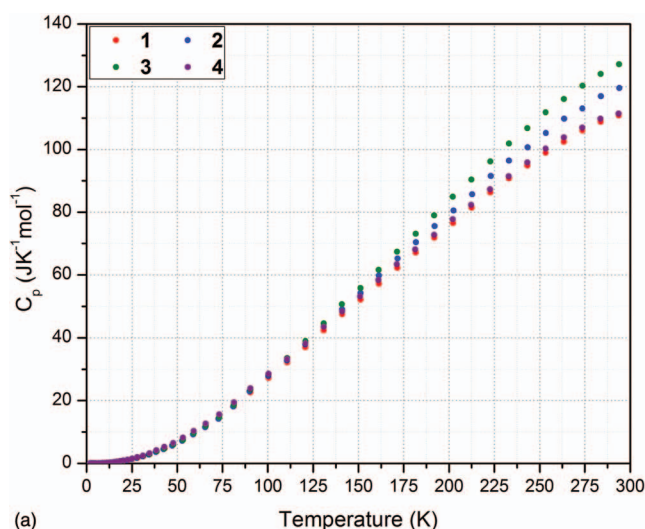

FIG. 3. Molar isobaric heat capacity (C_p) for the alumina nanoparticle samples **1–4**. These data were measured with the PPMS calorimeter. (a) C_p over the 2—300 K temperature range; (b) expansion of the <10 K temperature region of the C_p plot in (a).

form:[49]

$$C_{DE} = n_D D(\theta_D) + n_E E(\theta_E) + aT + bT^2, \quad (6)$$

where θ_D and θ_E are the Debye and Einstein temperatures, respectively. The Debye [$n_D D(\theta_D)$] and Einstein functions [$n_E E(\theta_E)$] are representative of the isochoric heat capacity (C_v). The conversion between C_v and C_p can be performed with the following expression:

$$C_p = C_v + \alpha^2 KVT. \quad (7)$$

However, as values for the coefficient of expansion (α), bulk modulus (K), and molar volume (V) are not readily available for alumina nanoparticles it is necessary to approximate the conversion factor $\alpha^2 KVT$ with the terms aT and bT^2 (Eq. (6)).[49]

The total heat capacity of the alumina nanoparticles is equal to the sum of Eqs. (4)–(6). The various parameters derived from the least-squares fitting of these expressions to the C_p data for samples **1**–**4** are listed in Table II. Tables of C_p data and figures of the best-fit curves are provided in the supplementary material.[63]

The non-zero values for the γ coefficients are necessitated by the defect spinel structure of the γ-Al_2O_3 particles. The general formula for spinel materials with ideal stoichiometry is $(A^{2+})(B^{3+})_2O_4$, e.g., $MgAl_2O_4$. The dications (A^{2+}) of the spinel reside in the tetrahedral sites (T_d) of the crystalline lattice, and the trivalent cations (B^{3+}) occupy the octahedral sites (O_h). In the case of γ-Al_2O_3 all divalent cations are replaced with trivalent Al^{3+} ions. Consequently, it is essential

that vacant sites be incorporated within the γ-Al_2O_3 lattice to satisfy the Al_2O_3 stoichiometry and ensure charge balance. Thus, the chemical formula of γ-alumina is best expressed as $\square Al_8O_{12}$ (where $\square$ is a vacancy).

Theoretical calculations by Vijay *et al.* suggest that the vacancies with the γ-Al_2O_3 lattice are thermodynamically more stable when evenly distributed within the bulk of the lattice rather than situated on the oxide surface; moreover, it is energetically more favourable for the O_h sites to accommodate the vacancies rather than the T_h sites.[50] However, these authors also concede that the kinetic barrier for surface → bulk migration of the vacancies is high (1 eV) and therefore the vacancy distribution within the γ-Al_2O_3 lattice is essentially fixed during the synthesis of the particles. Furthermore, in this computational study the stabilizing influence of water on the γ-Al_2O_3 surface was neglected. Therefore, we cannot say with any certainty where the spinel vacancies reside within our alumina samples. However, the similarity in the magnitudes of the γ coefficients for **1**–**4** would imply that the vacancy concentrations are similar for all four samples.

Sohlberg and co-workers have proposed an alternative description for the chemical composition of γ-alumina.[51] These authors hypothesize, based on theoretical calculations, that γ-Al_2O_3 sequesters protons generating a "perfect" spinel devoid of vacancies with the chemical composition HAl_5O_8. If this were indeed the case then the γT term in the heat capacity expression that successfully models our alumina C_p data would be negligible, which it is not. These authors portray γ-alumina as "a reactive sponge" that causes the dissociation of water molecules at its surface. They speculate that the protons generated from this dissociation migrate into the bulk of the oxide and that the O^{2-} ions remain bound to the surface where they subsequently bind with Al^{3+} ions that migrate from the bulk to the surface, and in this manner the oxide lattice is said to extend. The authors rationalize that the loss of water that occurs when γ-alumina is heated is a result of the counter-migration and recombination the protons/oxide ions. Sohlberg *et al.* rule out the possibility that H_2O and OH species may be physically and/or chemically bound to the alumina surface where it may satisfy the valence requirements of the oxide and be the source of water removed during the dehydration of γ-Al_2O_3. Unfortunately, such considerations would undermine the probability that their proposed proton migration mechanism is realistic. Yet, our high-energy INS spectra of alumina samples **1**–**4** (discussed in detail below) clearly display peaks at ~205 meV that are characteristic of the bending modes of molecular water, and thus provide direct evidence of the existence of water on the surface of γ-Al_2O_3. Indeed, we have performed numerous INS studies of hydrated metal oxide nanoparticles and can only conclude based on the extensive experimental evidence available that both physisorbed water and chemically bound surface hydroxyl groups are integral components of such metal-oxide materials, especially at the nanoscale.[52–58]

Above ~110 K the C_p data for **1**–**4** begin to diverge, and as the temperature increases the separation between the data become more pronounced. As the curves for **1** and **4** are similar, even at these higher temperatures, this effect does
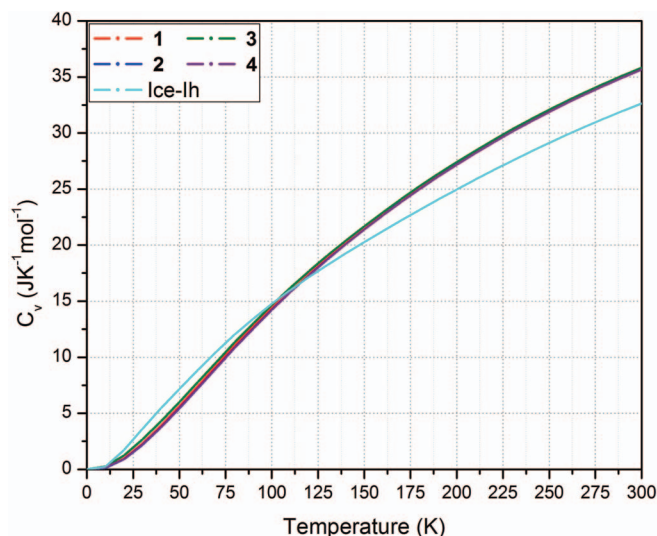
TABLE II. Refined parameters for the C_p curve fits applied to the specific heat capacity (C_p) data for **1**–**4**.

	1	2	3	4
C_{Lat} Parameter				
γ	0.001354	0.001391	0.00122	0.001391
B_3	7.8×10^{-5}	6.83×10^{-5}	0.000115	8.9×10^{-5}
B_5	-2.4×10^{-7}	1.73×10^{-7}	-9.0×10^{-7}	1.08×10^{-7}
B_7	2.36×10^{-9}	0	6.76×10^{-9}	0
$B_{(n>7)}$	0	0	0	0
%RMS	2.148113	1.948603	2.215441	0.948400
Polynomial parameter				
k_0	-0.01351	0.002294	-0.00533	-0.00634
k_1	0.012155	0.005835	0.012561	0.009815
k_2	-0.00275	-0.00201	-0.00358	-0.00257
k_3	0.000342	0.000325	0.000473	0.000374
k_4	-9.3×10^{-6}	-9.5×10^{-6}	-1.5×10^{-5}	-1.1×10^{-5}
k_5	1.19×10^{-7}	1.27×10^{-7}	2.04×10^{-7}	1.41×10^{-7}
k_6	-5.8×10^{-10}	-6.3×10^{-10}	-1.0×10^{-9}	-7.0×10^{-10}
$k_{(n>6)}$	0	0	0	0
%RMS	0.837521	1.365266	1.470125	1.157250
C_{DE} Parameter				
n_D	3.910934	3.393564	3.693941	4.013503
$D(\theta_D)$	606.6127	594.5814	591.8142	598.6377
n_E	8.042023	5.038065	7.289343	9.213478
$E(\theta_E)$	1137.334	1070.669	1079.866	1147.206
a	0.081918	0.056437	0.061745	0.097168
b	-0.00067	-0.00013	-0.00036	-0.00084
%RMS	0.486407	0.679317	0.677786	0.511975

FIG. 4. Isochoric heat capacity (C_v) for the hydration layers situated on the surface of alumina nanoparticles. These curves are calculated from the VDOS determined from the low energy TOSCA INS spectra recorded for samples **1–4**.

FIG. 5. VDOS for samples **1–4** calculated from the low-temperature high resolution INS spectra recorded on TOSCA. These curves have been displaced relative to each other to enable their features to be more easily seen. Also shown in the VDOS for the reference material ice–Ih.[39]

not seem to originate from differences in the pore diameter or the water content of the samples. At these temperatures the C_p data are modelled with a combined Debye-Einstein function, and this would suggest the observed divergence is a consequence of variations in the phonon distribution within the particles; unfortunately, our data does not allow for determination of the nature of these differences or their possible origin.

The isochoric heat capacity (C_v) for the hydration layers of the alumina nanoparticles can be calculated from the VDOS [$v(\omega)$] with the following expression:[59]

$$C_v = R \cdot \int_0^\infty \frac{v(\omega)(\hbar\omega/kT)^2 \exp(\hbar\omega/kT)}{[\exp(\hbar\omega/kT) - 1]^2} d\omega, \qquad (8)$$

where R is the universal gas constant (8.314 J mol^{-1} K^{-1}) and ω is the phonon angular frequency (s^{-1}). The results of these calculations are depicted in Fig. 4.

The C_v curves for all four hydrated γ-alumina samples are equivalent. The fact that the curves are equivalent in magnitude and structure can be traced to the similarity in the energy distributions of the translational (<40 meV) and librational bands (50–120 meV) of the VDOS for **1–4** (Fig. 5).[39] This implies that neither the pore size nor the water content of the sample influences the vibrational behaviour of the surface water species (*vide infra*). Below 110 K the heat capacity of the confined water is less than that for the reference material ice–Ih, this is a consequence of the redistribution of the translational modes to higher energy in the VDOS of the hydrated nanoparticles. Conversely, above 110 K the heat capacity of the surface water exceeds that of ice–Ih, and this can be rationalized by the occurrence of additional librational modes spanning the 40–65 meV region of the nanoparticle VDOS that are absent in the ice–Ih VDOS. These additional modes are indicative of softening of the librational modes of water on the nanoparticle surface.
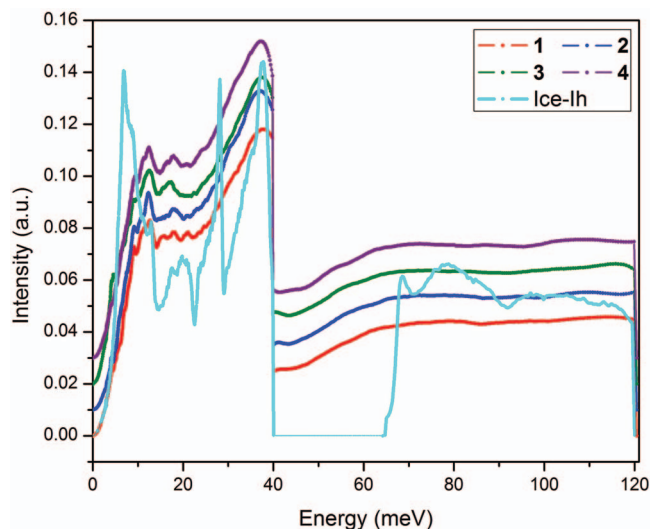
C. Dynamics of the confined water layers

Figure 6 displays INS spectra for **1–4** over the 0–600 meV energy range. Dinge *et al.* have conducted an extensive density functional theory (DFT) evaluation of the most prominent hydrated γ-alumina crystal surfaces.[45] This study allows us to conclude that the features at 390–470 meV (3145–3700 cm^{-1}) in the INS spectra of the hydrated alumina nanoparticles are most likely to be fundamental bands originating from the stretching vibrations of multi-coordinated H_2O and OH groups bridging six-fold coordinated aluminium atoms (Al$_{VI}$) on the nanoparticle surfaces. The peaks centered at $\sim$205 meV (1694 cm^{-1}) are associated with the $\delta(H_2O)$ bending mode,[60] and the broadness of these peaks is probably caused by H_2O molecules experiencing a range of hydrogen bonding environments on the γ-alumina surface that result in modification of the H_2O bending energy.

The librational modes of the physisorbed molecular water can be seen spanning the 50–140 meV regions of the INS spectra. These modes are associated with the frustrated rotations of the molecules, and consequently they are particularly sensitive to the hydrogen bond networks in which the molecules participate. It is immediately apparent that the librational bands for all samples are featureless and broader relative to the equivalent band in the VDOS of ice–Ih, and this is indicative of the hydrogen bond network within the nanoparticle hydration layers being distorted relative to that in ice–Ih. This softening of the librational motion of the water molecules can be explained by weaker hydrogen bonds between the water molecules confined to the nanoparticle surface relative to those in ice–Ih. Furthermore, the high-energy region of this band is probably due to vibrations of the protons within the hydroxyl group in the plane normal to the O–H bond.

The translation modes (observed at <40 meV in the INS spectra) of the water molecules confined to the alumina surfaces are strongly restricted relative to those molecules in
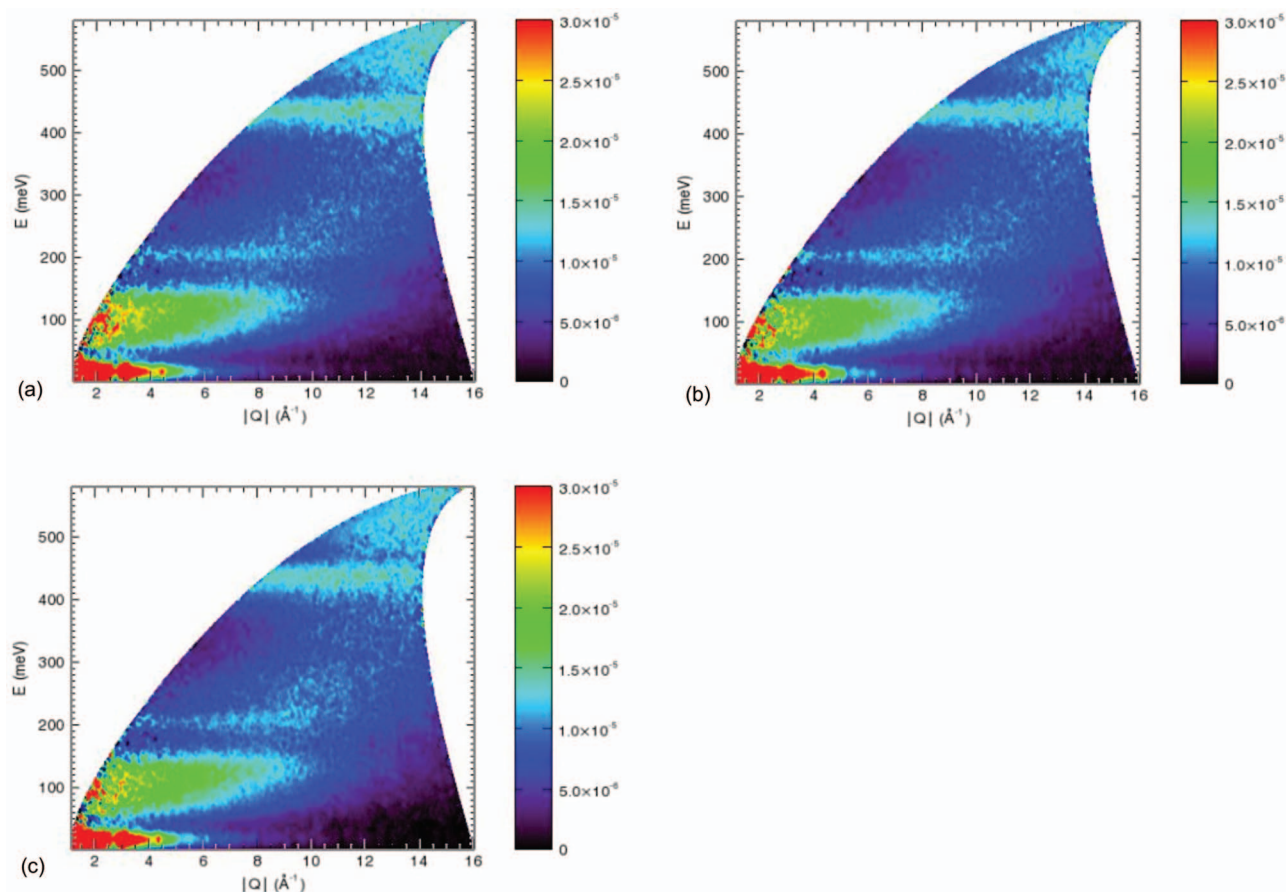
FIG. 6. INS spectra [G(E)] for samples **1** (a), **3** (b), and **4** (c). These data we recorded at low temperature (7 K) on SEQUIOA with $E_i = 600$ meV.

ice–Ih, this is most evident for translational mode that occurs at 7 meV in the VDOS of ice–Ih that is shifted to higher energy (12 meV) and suppressed in intensity in the VDOS of **1**–**4**. This restriction is undoubtedly due to the presence of strong surface-water interactions facilitated by hydrogen bonding between the H_2O molecules and the oxygen atoms and chemisorbed OH groups on the γ-alumina surface. It is also noticeable that the translational bands of the nanoparticle VDOS are less structured than that of ice–Ih, which suggests that the water environment is more isotropic on the nanoparticle surface than in the crystalline lattice of ice–Ih.

If we assume that the effective surface area for an adsorbed water molecule is 0.14 nm^2,[61] then for monolayer coverage approximately seven molecules of water populate 1 nm^2 of particle surface. Thus, based on the surface coverage values reported in Table I the nanoparticle samples employed in this study have between one and two layers of water on their surfaces. Based on the results from an in-depth transmission FT–IR study Abadleh and Grassian postulated that the surface of alumina particles is terminated with OH groups generated from the dissociation of molecular water, and these chemically bound hydrophilic groups constitute the first layer of water species on the surface.[60] The second hydration layer is constructed from an ordered array of water molecules hydrogen bonded to the surface hydroxyl groups. Our INS results concur with these findings and provide additional evidence for the existence of both surface OH groups and molecular water in powdered γ-alumina systems. A

detailed examination of the low energy region of the SEQUOIA data (Fig. 7) shows well-defined vibrational peak at 115 meV [ν_1(OH)] that provide clear evidence for the presence of hydroxyl groups bound to the surface of the alumina particles (this peak is also seen in the TOSCA data, see
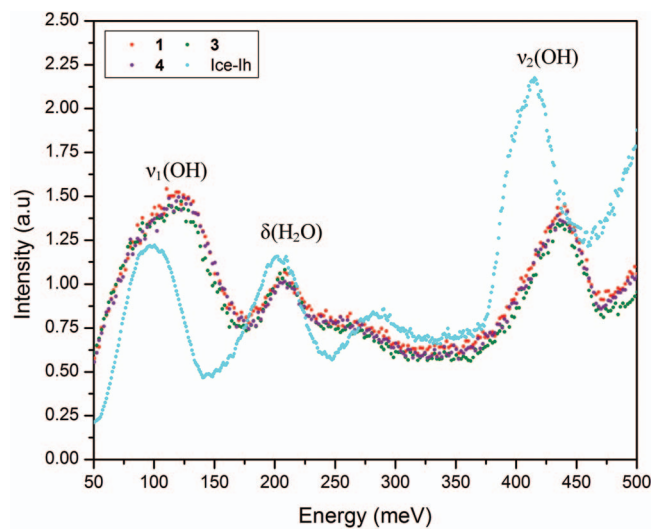

FIG. 7. Detailed INS spectra [G(E)], summed over the 2–14 Å^{-1} for samples **1**, **3**, **4**. These data were measured on SEQUIOA. Also shown for the purpose of comparison is the spectrum for the reference material ice–Ih. The key excitations that relate to the structure of the nanoparticle hydration layers are labelled.

Fig. S2 in the supplementary material).[63] Additionally, there are bands evident at ∼440 meV (Figs. 6 and 7) associated with the stretching modes of these OH groups. The peaks at ∼440 meV in the spectra for **1**–**4** are shifted significantly relative to the related peak in the ice–Ih spectrum (at ∼410 meV), and this is indicative of these hydroxyl groups participating in weak hydrogen bonding with neighbouring water species. This proposed structural model for the surface water on alumina closely resembles that determined from INS data for hydrated PdO nanoparticles.[62] Furthermore, the similarity of the spectra for **1**–**4** implies that the pore size does not affect the structure of the surface hydration layers, and only the particle on which they reside influences the dynamics of the water species.

To obtain an approximate ratio for the number of hydroxyl groups to molecular water molecules present on the surface of the alumina nanoparticles the $\delta(H_2O)$ peak at ∼205 meV and the $\nu_2(OH)$ stretching peak at ∼440 meV in the spectra of **1** were fitted with Gaussian functions (Fig. S6, SI). The same procedure was performed for the equivalent peaks in the ice–Ih spectrum. The ratios of the integrated intensities of the $\nu_2(OH)$ and $\delta(H_2O)$ peaks were 2.98 and 1.57 for **1** and ice–Ih, respectively. Consequently, as the alumina ratio is approximately twice that of ice–Ih we can conclude that ratio of protons within the OH groups and H_2O molecules on the surface of the nanoparticles is 1:1, this reveals that there are approximately double the number of OH groups chemically bound to the surface of the alumina particles as there are physisorbed H_2O molecules. It should also be noted that our rationale for evaluating the ratio of peak intensities is that there is a strong contribution from multi-phonon and multiple neutron scattering events to the spectra that are difficult to correct for, and these will be different for ice–Ih and the sample spectra. Thus, quantitative estimates of the peak intensities will be inaccurate.

IV. CONCLUSION

By combining both calorimetric and INS techniques we have explored in detail the thermodynamic properties of γ-Al_2O_3 nanoparticles and evaluated the dynamical behaviour of the stabilising water layers confined to their surface. From this comprehensive study the following key conclusions can be drawn: (i) As frequently observed in metal oxide nanoparticle systems the γ-Al_2O_3 surface is terminated by multi-coordinated chemically bound OH and H_2O species, and further stabilised by physisorbed molecular water; (ii) The C_p data support the hypothesis that cation vacancies are occluded within the γ-Al_2O_3 lattice, although their concentration and distribution are unknown; (iii) Neither the water content of the alumina nanopowder nor the pore diameter impacts on the thermodynamic properties of the γ-alumina nanoparticles; (iv) The water species confined to the alumina surfaces are strongly bound by an extensive network comprising both covalent and hydrogen bonds. These interactions act to restrict the motion of these groups, and consequently the energy distribution of the rotational and translational modes of the surface water is modified relative to ice–Ih.

[1]J. M. McHale, A. Auroux, A. J. Perrota, and A. Navrotsky, Science **277**, 788–791 (1997).
[2]A. Navrotsky, Geochem. Trans. **4**, 34–37 (2003).
[3]I. Levin and D. Brandon, J. Am. Ceram. Soc. **81**, 1995–2012 (1998).
[4]S. J. Smith, S. Amin, B. F. Woodfield, J. Boerio-Goates, and B. J. Campbell, Inorg. Chem. **52**, 4411–4423 (2013).
[5]Z. Łodziana, N.-Y. Topsøe, and J. K. Nørskov, Nat. Mater. **3**, 289–293 (2004).
[6]P. J. Eng, T. P. Trainor, G. E. Brown, Jr., G. A. Waychunas, M. Newville, S. R. Sutton, and M. L. Rivers, Science **288**, 1029–1033 (2000).
[7]J. M. McHale, A. Navrotsky, and A. J. Perrotta, J. Phys. Chem. B **101**, 603–613 (1997).
[8]M. Kole and T. K. Dey, Exp. Therm. Fluid Sci. **34**, 677–683 (2010).
[9]G. Malucelli, P. Palmero, S. Ronchetti, A. Delmastro, and L. Montanaro, Polym. Int. **59**, 1084–1089 (2010).
[10]T. Joshi, J. Prakash, A. Kumar, J. Gangwar, A. K. Srivastava, S. Singh, and A. M. Biradar, J. Phys. D **44**, 315404 (2011).
[11]D. Jiao, S. Zheng, Y. Wang, R. Guan, and B. Cao, Appl. Surf. Sci. **257**, 5720–5725 (2011).
[12]S. Radice and S. Mischler, Wear **261**, 1032–1041 (2006).
[13]H. Lei, N. Bu, R. Chen, P. Hao, S. Neng, X. Tu, and K. Yuen, Thin Solid Films **518**, 3792–3796 (2010).
[14]H. Lei and P. Zhang, Appl. Surf. Sci. **253**, 8754–8761 (2007).
[15]A. Afkhami, M. Saber-Tehrani, and H. Bagheri, J. Haz. Mater. **181**, 836–844 (2010).
[16]Y. C. Sharma, V. Srivastava, S. N. Upadhyay, and C. H. Weng, Ind. Eng. Chem. Res. **47**, 8095–8100 (2008).
[17]A. K. Patra, A. Dutta, and A. Bhaumik, J. Haz. Mater. **201–202**, 170–177 (2012).
[18]A. Kaur and U. Gupta, J. Mater. Chem. **19**, 8279–8289 (2009).
[19]S. Boullosa-Eiras, T. Zhao, D. Chen, and A. Holmen, Catal. Today **171**, 104–115 (2011).
[20]Z. Suo, C. Ma, M. Jin, T. He, and L. An, Catal. Commun. **9**, 2187–2190 (2008).
[21]J. Yin, J. Wang, T. Zhang, and X. Wang, Catal. Lett. **125**, 76–82 (2008).
[22]G. P. Rachiero, U. B. Demirci, and P. Miele, Catal. Today **170**, 85–92 (2011).
[23]R. Chakravarty, R. Shulka, R. Ram, M. Ventatesh, A. K. Tyagi, and A. Dash, Anal. Chem. **83**, 6342–6348 (2011).
[24]B. F. Woodfield, S. Liu, J. Boerio-Goates, and Q. Liu, U.S. patent 8,211,388 (2012).
[25]B. F. Woodfield, S. Liu, J. Boerio-Goates, and Q. Liu, "Preparation of uniform nanoparticles of ultra-high purity metal oxides, mixed metal oxides, metals, and metal alloys," U.S. patent 8,211,388, E.U. patent 1,986,804 (2012).
[26]B. Huang, C. H. Bartholomew, S. J. Smith, and B. F. Woodfield, Micropor. Mesopor. Mater. **165**, 70–78 (2013).
[27]B. Huang, C. H. Bartholomew, and B. F. Woodfield, Micropor. Mesopor. Mater. **183**, 37–47 (2014).
[28]B. Huang, C. H. Bartholomew, and B. F. Woodfield, Micropor. Mesopor. Mater. **177**, 37–46 (2013).
[29]S. J. Gregg and K. S. W. Sing, *Adsorption, Surface Area and Porosity*, 2nd ed. (Academic Press, London, 1982).
[30]F. Rouquerol, J. Rouquerol, and K. Sing, *Adsorption by Powders and Porous Solids* (Academic Press, London, 1999).
[31]Q. Shi, C. L. Snow, J. Boerio-Goates, and B. F. Woodfield, J. Chem. Thermodyn. **42**, 1107–1115 (2010).
[32]B. Huang, C. H. Bartholomew, and B. F. Woodfield, Micropor. Mesopor. Mater. **184**, 112–121 (2014).
[33]Q. Shi, J. Boerio-Goates, and B. F. Woodfield, J. Chem. Thermodyn. **43**, 1263–1269 (2011).

[34] P. C. Mitchell, S. F. Parker, A. J. Ramirez–Cuesta, and J. Tomkinson, *Vibrational Spectroscopy with Neutrons with Applications in Chemistry, Biology, Materials Science and Catalysis* (World Scientific Publishing Co. Pt. Ltd., 2005).

[35] G. L. Squires, *Introduction to the Theory of Thermal Neutron Scattering* (Cambridge University Press, 1978).

[36] W. Marshall and S. W. Lovesey, *Theory of Thermal Neutron Scattering* (Clarendon Press, Oxford, 1971).

[37] S. W. Kieffer, Rev. Geophys. Space Phys. **17**, 1–19, doi:10.1029/RG017i001p00001 (1979).

[38] P. Richet, *The Physical Basis of Thermodynamics with Applications to Chemistry* (Kluwer Academic/Plenum Publishers, New York, 2001).

[39] J. Li and A. I. Kolesnikov, J. Mol. Liq. **100**, 1–39 (2002).

[40] G. E. Granroth, D. H. Vandergriff, and S. E. Nagler, Physica B **385–386**, 1104–1106 (2006).

[41] G. E. Granroth, A. I. Kolesnikov, T. E. Sherline, J. P. Clancy, K. A. Ross, J. P. C. Ruff, B. D. Gaulin, and S. E. Nagler, J. Phys.: Conf. Ser. **251**, 012058 (2010).

[42] T.-J. Park, A. A. Levchenko, H. Zhou, S. S. Wong, and A. Navrotsky, J. Mater. Chem. **20**, 8639–8645 (2010).

[43] A. Navrotsky, Int. J. Quantum Chem. **109**, 2647–2657 (2009).

[44] X. Liu, G. Qiu, and X. Li, Nanotechnology **16**, 3035–3040 (2005).

[45] M. Digne, P. Sautet, P. Raybaud, P. Euzen, and H. Toulhoat, J. Catal. **226**, 54–68 (2004).

[46] R. H. R. Castro and D. V. Quach, J. Phys. Chem. C **116**, 24726–24733 (2012).

[47] V. I. Petinov, Tech. Phys. **57**, 302–304 (2012).

[48] J. Majzlan, A. Navrotsky, B. F. Woodfield, B. E. Lang, J. Boerio-Goates, and R. A. Fisher, J. Low Temp. Phys. **130**, 69–76 (2003).

[49] S. J. Smith, R. Stevens, S. Liu, G. Li, A. Navrotsky, J. Boerio-Goates, and B. Woodfield, Am. Mineral. **94**, 236–243 (2009).

[50] A. Vijay, G. Mills, and H. Metiu, J. Chem. Phys. **117**, 4509–4516 (2002).

[51] K. Sohlberg, S. J. Pennycook, and S. T. Pantelides, J. Am. Chem. Soc. **121**, 7493–7499 (1999).

[52] Q. Shi, J. Boerio-Goates, K. Woodfield, M. Rytting, K. Pulsipher, E. C. Spencer, N. L. Ross, A. Navrotksty, and B. F. Woodfield, J. Phys. Chem. C **116**, 3910–3917 (2012).

[53] A. A. Levchenko, G. Li, J. Boerio-Goates, B. F. Woodfield, and A. Navrotsky, Chem. Mater. **18**, 6324 (2006).

[54] E. C. Spencer, N. L. Ross, S. F. Parker, A. I. Kolesnikov, B. F. Woodfield, K. Woodfield, M. Rytting, J. Boerio-Goates, and A. Navrotsky, J. Phys. Chem. C **115**, 21105–21112 (2011).

[55] N. L. Ross, E. C. Spencer, A. A. Levchenko, A. I. Kolesnikov, D. L. Abernathy, J. Boerio-Goates, B. F. Woodfield, A. Navrotsky, G. Li, W. Wang, and D. J. Wesolowski (Mater. Res. Soc. Symp. Proc., 2011), Vol. 1352.

[56] E. C. Spencer, N. L. Ross, S. F. Parker, B. F. Woodfield, J. Boerio-Goates, S. J. Smith, R. E. Olsen, A. I. Kolesnikov, A. Navrotsky, and C. Ma, J. Phys.: Condens. Matter. **23**, 205303 (2011).

[57] E. C. Spencer, A. A. Levchenko, N. L. Ross, A. I. Kolesnikov, J. Boerio–Goates, B. F. Woodfield, A. Navrotsky, and G. Li, J. Phys. Chem. A **113**, 2796–2800 (2009).

[58] E. C. Spencer, S. F. Parker, and N. L. Ross, J. Chem. Thermodyn. **51**, 103–106 (2012).

[59] All numerical integration procedures were performed with Origin v8, OriginLab Corporation, MA, U.S.A., 1991–2007.

[60] H. A. Al-Abadleh, and V. H. Grassian, Langmuir **19**, 341–347 (2003).

[61] M. V. Šušić, D. R. Vučelić, S. V. Paušak, D. B. Karaulić, and V. Milaković-Vučelić, J. Phys. Chem. **73**, 1975–1984 (1969).

[62] S. F. Parker, K. Refson, A. C. Hannon, E. R. Barney, S. J. Robertson, and P. Albers, J. Phys. Chem. C **114**, 14164–14172 (2010).

[63] See supplementary material at http://dx.doi.org/10.1063/1.4850636 for TGA curves, raw INS spectra, PD-XRD diffractograms, PSD curves, C_p data in tabular format, best-fit curves for modelling the C_p data, and fits to selected peaks in the high-energy region of the INS data, additional TEM images.